GDCh

Research Articles

Angewandte
Chemie
International Edition
www.angewandte.org

Organic Electronics | Hot Paper

Modular Nitrogen-Doped Concave Polycyclic Aromatic Hydrocarbons for High-Performance Organic Light-Emitting Diodes with Tunable Emission Mechanisms**

Jakub Wagner[+], Paola Zimmermann Crocomo[+], Michał Andrzej Kochman[+], Adam Kubas,* Przemysław Data,* and Marcin Lindner*

Dedicated to Professor Klaus Müllen on the occasion of his 75th birthday

Abstract: Although bowl-shaped N-pyrrolic polycyclic aromatic hydrocarbons (PAHs) can achieve excellent electron-donating ability, their application for optoelectronics is hampered by typically low photoluminescence quantum yields (PLQYs). To address this issue, we report the synthesis and characterization of a series of curved and fully conjugated nitrogen-doped PAHs. Through structural modifications to the electron-accepting moiety, we are able to switch the mechanism of luminescence between thermally activated delayed fluorescence (TADF) and room-temperature phosphorescence (RTP), and to tune the overall PLQY in the range from 9% to 86%. As a proof of concept, we constructed solid-state organic light-emitting diode (OLED) devices, which has not been explored to date in the context of concave N-doped systems being TADF/RTP emitters. The best-performing dye, possessing a peripheral trifluoromethyl group adjacent to the phenazine acceptor, exhibits yellow to orange emission with a maximum external quantum efficiency (EQE) of 12%, which is the highest EQE in a curved D-A embedded N-PAH to date.

Introduction

Polycyclic aromatic hydrocarbons (PAHs)[1–3] designed within the last two decades find use in a number of applications, including as chemical sensors,[4] organic field-effect transistors (OFETs),[5] organic solar cells,[6] fluorescence imaging labels,[7,8] liquid crystals,[9,10] and organic light-emitting diodes (OLEDs).[11] One of the most fruitful approaches to tuning their physicochemical properties is doping with elements other than carbon, either at the periphery of the molecule, or within the polycyclic system. The dopant atoms alter both the electronic properties, such as the MO energy levels, and molecular geometry. This latter factor is of particular importance for nitrogen-doped PAHs.[12,13] A centrally positioned N-heteroatom surrounded solely by six-membered rings leads to various planar or only slightly bent architectures, such as the carbonyl-, dimethyl-, O-, and S-bridged N-heterotriangulenes (Figure 1a, structures **1**–**4b**).[14–17] Even though the latter examples prove to be strong electron donors, their relatively poor thermal and chemical stabilities, and strong tendencies towards π-stacking interactions, impede their practical application.

Conversely, when the N-dopant is partially or fully surrounded by five- and/or seven-membered rings, the ring system adopts a concave, or bowl-shaped geometry. In turn, the curvature of the molecular skeleton has a strong effect on the photophysical properties of the N-doped PAHs.[12,13] In contrast to their planar analogues, relatively few examples of π-extended N-embedded PAHs (selected examples are shown in Figure 1b) have been reported thus far, as their preparation typically requires tedious and multistep syntheses. Notably, seminal works on the pyrrole-embedded curved PAHs **5a** and **5b** were independently reported by Nozaki[18] and Shinokubo;[19] whereas further modifications of this scaffold were explored by Ito[20,21] and Feng.[22] More recently, Zhang and co-workers reported PAHs containing acridone (**6** and **7**)[23–25] and phenothiazine (**8**)[26], as suitable building blocks to ensure the desired curvature for the construction of concave and boat-like conformations, respectively. Moreover, the Gryko research group demonstrated the utility of pyrrolo[3,2-b]pyrrole in forming a

[*] J. Wagner,[+] Dr. M. Lindner
Institute of Organic Chemistry, Polish Academy of Sciences
Kasprzaka 44/52, 01-224 Warsaw (Poland)
E-mail: mlindner@icho.edu.pl

Dr. M. A. Kochman,[+] Dr. A. Kubas
Institute of Physical Chemistry, Polish Academy of Sciences
Kasprzaka 44/52, 01-224 Warsaw (Poland)
E-mail: akubas@ichf.edu.pl

P. Zimmermann Crocomo,[+] Prof. P. Data
Faculty of Chemistry, Silesian University of Technology
M. Strzody 9, 44-100 Gliwice (Poland)
E-mail: przemyslaw.data@polsl.pl

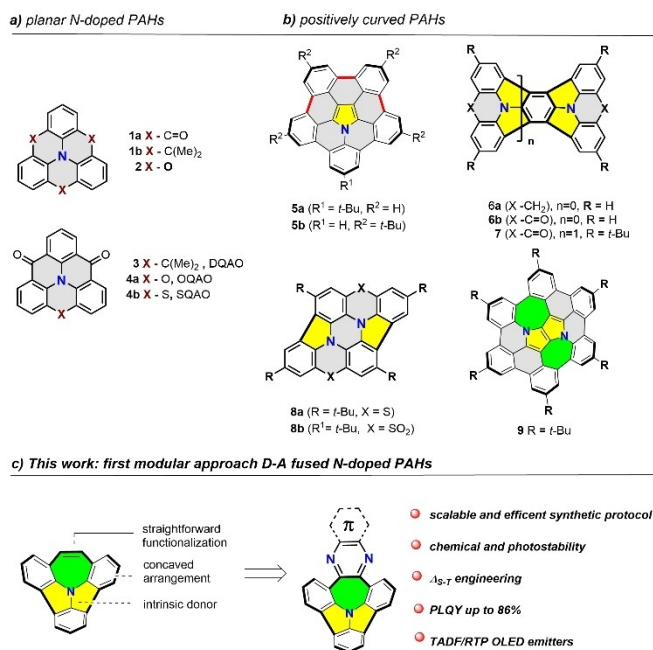[+] These authors contributed equally to this work.

Figure 1. Chemical evolution of N-doped PAHs.

buckybowl-like system, with inverse Stone–Thrower–Wales defects, first through "on surface",[27] and subsequently "in solution"[28] approaches (Figure 1b, **9**). Despite the promising structural alignment of an electron-donating group (D), exploration of curved N-PAHs as prospective optoelectronic materials is limited by their relatively low emission efficiency. The tailoring of their band gaps and singlet–triplet (S-T) states through modification of the periphery of the π-scaffold is the most straightforward method to optimize these properties. However, this approach is complicated by the need to attach solubilizing groups in what are often the most reactive positions of N-PAHs, which prevents further synthetic transformations with electron-accepting species (A). Partially for this reason, the rational design of non-planar and thoroughly conjugated N-PAHs with a D-A electronic structure that compensates for the desired functions and synthetic availability has remained elusive.

The phenomenon of thermally activated delayed fluorescence (TADF) shows great promise for the enhancement of the external quantum efficiencies (EQEs) of organic light-emitting diodes (OLEDs). In principle at least, TADF-active organic emitters can quantitatively harvest the excitons generated in the emitting layer through electrical excitation and convert them into light through efficient reverse intersystem crossing (rISC).[29–32] The key issue in designing efficient TADF emitters is the acceleration of a spin-forbidden and endothermic rISC process $(T_1 \rightarrow S_1)$. D-A π-conjugated systems with a sizeable D-A dihedral angle and vibrational motion achieve this by minimizing the singlet-triplet energy gap ($\Delta E_{ST} < 0.2$ eV) to lower the activation energy for rISC and mixing excited charge-transfer (CT) and localized energy (LE) states to allow spin-flip electronic transitions. Therefore, the development of TADF active organic materials has so far relied on

planar and branched D-A species. A significant drawback of this architecture is that the radiative emission cross-sections are typically small. This effect adversely influences photoluminescence quantum yield (PLQY). On the other hand, when a moderate ΔE_{ST} (0.3–0.6 eV) is identified, in competition with TADF, photon emission can take place through room-temperature phosphorescence (RTP).[33] Consequently, the molecular design targeted strictly at TADF or RTP is fundamentally important from the viewpoint of future applications in the domains of sensors, data encryption, and white light-emitting OLEDs (WOLEDs).[34]

Herein, we report a concise and efficient synthetic strategy towards a new class of nonplanar N-PAHs with intrinsic D-A electronic structures which are, for the first time, applied as yellow to orange TADF/RTP OLED emitters (Figure 1c). These compounds owe their attractive photophysical properties, such as the spatial separation of the HOMO and the LUMO, to an antiaromatic seven-membered ring located between the electron-donating and -accepting moieties. The entirely fused, and curved system leads to the small Δ_{S-T} energy and enables control of the emission mechanisms (TADF vs RTP) with respect to the acceptor applied. Their strength contributes to the remarkable PLQY amplification (up to 86%) determined for the most electron-poor derivative. Thus, the OLEDs fabricated with the developed N-PAHs as TADF/RTP emitters are unprecedented for this class of compounds and can achieve an EQE as high as 12% along with satisfactory operational stability and a low roll-off process.

Results and Discussion

We envisaged our ambipolar N-PAHs as suitable architectures for TADF/RTP emitters because of the built-in separation of frontier molecular orbitals (FMOs) and thus adjusting S–T energy levels (implementation of curvature could minimize FMOs overlap and narrow ΔE_{ST}). Thus, appropriate selection of building blocks is fundamental to simultaneously maintain (i) the desired curvature (caused by two pentagons and one heptagon) around an electron-donating nitrogen atom, (ii) insert an electron-poor unit on the periphery of PAHs so as to afford an efficient separation of orbitals. Taking this into account, we utilized commercially available dibenz[*b,f*]azepine to face the design requirements (i/ii). Therefore, the synthetic pathway demonstrated in Scheme 1 starts from its chemoselective Buchwald–Hartwig amination[35] with 2,6-dichloro-1-iodobenzene delivering amine **11** in excellent 89% yield. Subsequent annulation of two 5-membered rings by microwave-assisted direct arylation was achieved through modification of reaction conditions first reported by the Scott[36] group (only 5 mol% of Pd catalyst was implemented) in which the dichlorinated precursor was subjected to heating for 50 min to obtain compound **12** in 77% yield on a multigram scale. Inclusion of the antiaromatic (for a detailed discussion on the antiaromaticity of our N-PAHs, see the Supporting Information, section SI-10) seven-membered ring of azepine in this structure allows for further oxidation to diketone **13**. The
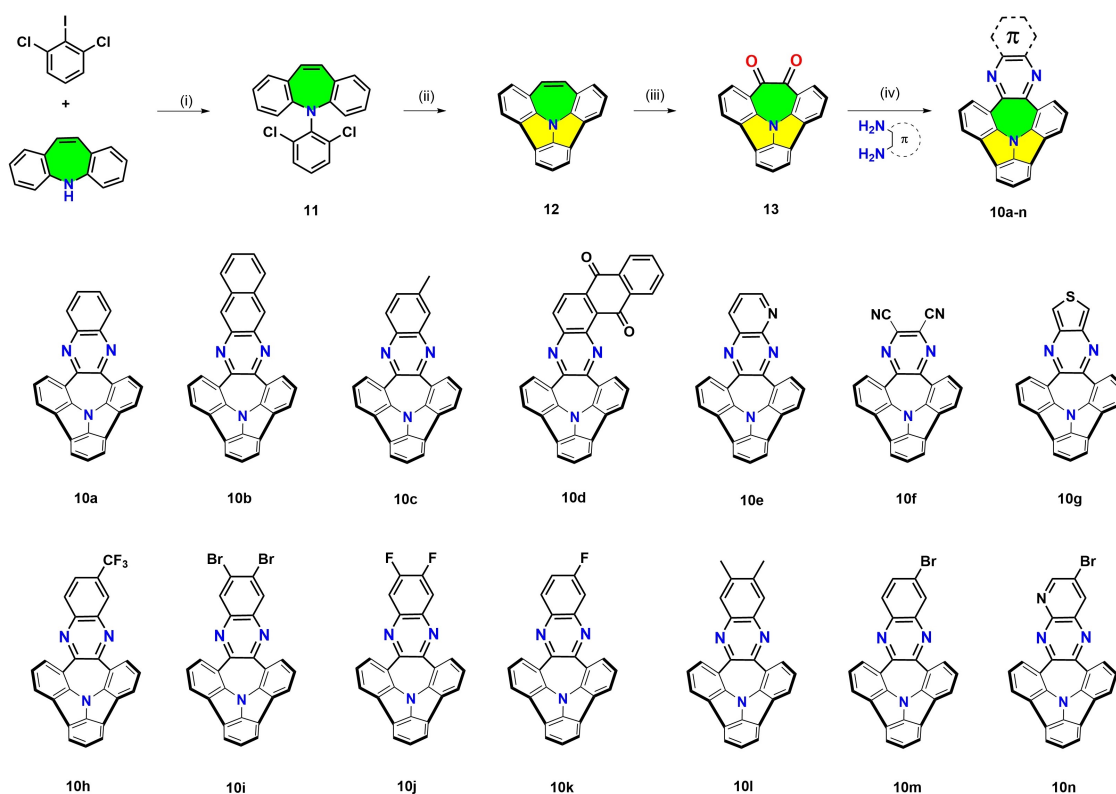
Scheme 1. The synthetic path towards D-A arranged N-PAHs with an array of electronically diverse phenazines. Reagents and conditions: (i) Pd(OAc)$_2$, P(tBu)$_3$HBF$_4$, NaOtBu, toluene; 89%. (ii) [Pd(Pcy)$_3$]Cl$_2$, DBU, DMAc, MW, 77%. (iii) RuCl$_3$, NaIO$_4$, NMI, THF/DCM/H$_2$O, 37% or BSA, o-dichlorobenzene, 65%. (iv) AcOH/EtOH, 1:1, 56–79%.

first oxidative approach we examined was that commonly used for the selective oxidation of pyrene-embedded PAHs.[37] Using this approach, the synthesis of the key intermediate **13** was achieved with an unsatisfying 37% yield. The use of benzeneseleninic acid anhydride (BSA)[38] proved significantly more effective, however, and the oxidation efficiency was raised to 65%. Planar analogues of dione **13** are known to readily undergo acid-promoted condensation with various 1,2-aromatic diamines to yield π-extended phenazines.[39] Accordingly, a series of 14 phenazine derivatives (**10a–10n**) were created from appropriate diamines to give curved N-PAH derivatives with a range of electron-accepting properties and points of further functionalization. Each synthetic step was found to be readily scalable, and three of them (Supporting Information, section SI-3) could be performed without chromatographic separation, which increases the prospective applicability of the current methodology. Incorporation of such a diverse range of fused phenazine derivatives with electronically varied substituents allows for strict control of the strength of the acceptor. With such molecular engineering, we anticipated that fine control of the optoelectronic features of our N-PAHs, such as a tunable emission mechanism (TADF vs RTP), could be achieved with a great emphasis on excited states energies.

Single crystals of **10l** suitable for single-crystal X-ray analysis were obtained by slow evaporation of a dichloromethane/tetrahydrofuran solvent mixture at room temperature. This compound crystallizes in the *P*-1 space group with two molecules in the unit cell. Analysis of the obtained structure, displayed in Figure 2, unambiguously confirmed the proposed concave geometry. The distance of the central nitrogen atom and the plane of the three carbon atoms of the peripheral benzene rings indicate the depth to be 0.63 Å (Figure 2b). The less pronounced depth of **10l** compared to **6b** and **7** is due to the lower strain produced by the seven-membered ring in the N-PAHs reported herein. This finding
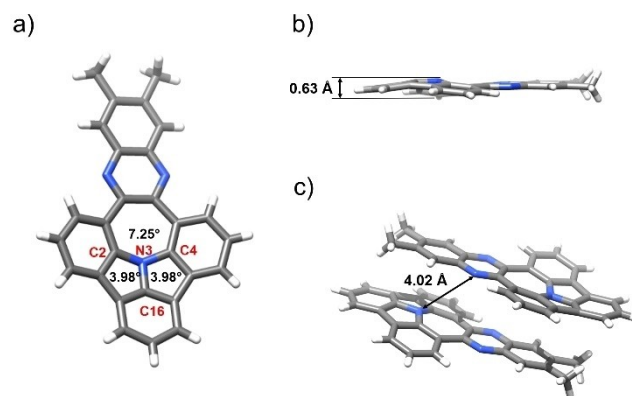

Figure 2. Crystal structure of **10l**: a) view of the crystal structure of **10l** from the concave face and POAV angles; b) side view of the crystal structure of **10l** with measured depth; c) the molecular packing in the crystalline state.

can be tracked with the π-orbital axis vector (POAV) angle (Figure 2b), that is a distinctive index for nonplanar compounds. In this consideration, the nitrogen POAV angle for **10l** (7.25°) was evaluated compared to those of **5a/b** ($\approx$7.55°)[18,19] and **6a/b**, **7**, and **9** (15°–16.4°).[23,24,28] An analogous deviation was measured for inner carbon atoms (C2, C4, C16) that occur in between 3.98°–5.25°.

Interestingly, nearly all previously reported curved systems[23–25] stack in a concave–convex manner assembled in the same direction, thus promoting undesirable π-π stacking. In contrast, molecules of compound **10l** in the crystal phase adopt a "head-to-tail" antiparallel arrangement. As can be seen in Figure 2c, the electron-donating group of one molecule in the unit cell is in contact with the electron-accepting group of the other molecule with almost parallel orientation of the D-A units. The short distances were measured to be 4.02 Å, which reveals a lack of unwanted π-π interactions (for further proof see the optical studies in solution, Supporting Information, section SI-5, Figure S21). This spatial arrangement of molecules in the crystal phase could promote the formation of excitons, which is advantageous from the standpoint of photophysics and possible applications in TADF/RTP OLEDs.

The crystal structure of **10l** presented the intended curvature of the designed molecular scaffold. In order to examine the relationship between the structures and the optical properties of compounds **10a–10n**, their electronic excitation spectra were simulated with second-order algebraic diagrammatic construction theory with spin-component scaling (SCS-ADC(2)).[40,41] For the sake of brevity, in the main body of our paper we focus on compound **10l** as a representative example. The vertical excitation energies for the other compounds in the series **10a–10n** are given in Table S2 (Supporting Information, section SI-2). The electronic structures of the low-lying excited states of compound **10l** were visualized by plotting electron density difference maps (EDDMs). An EDDM is defined simply as a difference between the electron density of the excited state and that of the ground state at the same nuclear geometry. Thus, the EDDM shows the redistribution of electron density associated with a given vertical transition. Figure 3 presents a summary of the simulation results. According to our calculations, the lowest singlet excited state (S_1) of compound **10l** is a $^1\pi\pi^*$-type state with a vertical excitation energy of 3.455 eV. The inspection of its EDDM (see the lower left panel of Figure 3) shows that this state has a partial donor-to-acceptor character. In the canonical MO picture, the S_1 state arises mainly from a HOMO→LUMO excitation. The S_0→S_1 transition is characterized by an appreciably large oscillator strength, considerably larger than the transitions into the other low-lying singlet excited states. Thus, the lowest photo-absorption band of **10l** can be assigned mainly to the transition into the S_1 state. In what follows, we refer to the analogous singlet CT-type states of compounds **10a–10n** simply as the ^{1}CT states. The S_1 state is closely followed by the S_2 state with a vertical excitation energy of 3.522 eV. The S_2 state is mainly localized on the donor group, as evidenced by its EDDM (see the upper left panel of Figure 3). It does not exhibit a significant CT character. In the canonical MO picture, this state arises predominantly from a HOMO→LUMO+1 excitation, with smaller contributions from other electronic configurations. The S_0→S_2 transition displays a relatively low oscillator strength. Other compounds in the series **10a–10n** exhibit
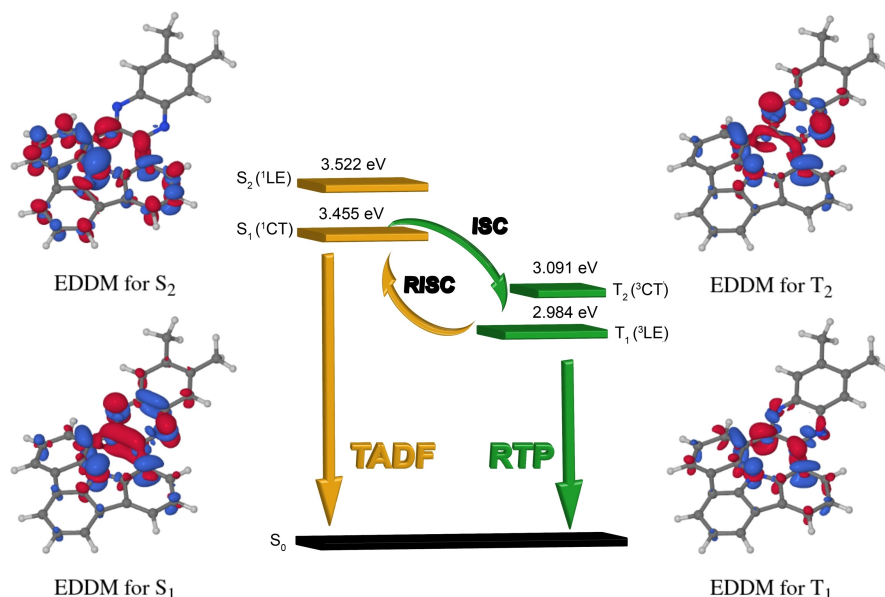

Figure 3. Energy level diagram for compound **10l**. The energy scale is qualitative. The main nonradiative transitions and luminescence processes are marked with arrows, while the insets on either side of the diagram show EDDMs for the relevant excited electronic states calculated at the ground-state equilibrium geometry. The EDDMs are plotted in the form of isosurfaces with isovalues of ± 0.002 e/a_0^3. The red and blue isosurfaces delimit regions in which the electron density is increased and decreased, respectively, relative to the S_0 state.

analogous low-lying non-polar $^1\pi\pi^*$-type states, and in what follows, we will refer to these as the ^{1}LE (locally excited) states. The S_3 and S_4 states, in turn, are energetically well-separated from the S_1 and S_2 states, and display low oscillator strengths for excitation from the ground state. For this reason, the S_3 and S_4 states are not expected to play a significant role in the photophysics of compound **10l**. The lowest two triplet states of compound **10l** (T_1 and T_2) found at 2.984 eV and 3.091 eV, respectively. Both these states exhibit pronounced multiconfigurational character, which is presumably because they lie close in energy and interact strongly with one another. We also located T_3 and T_4 states higher in energy, ca. 0.3 eV above the T_2 state. In most of the other compounds in the series **10a**–**10n**, the electronic structures of the S_1 and S_2 states are qualitatively similar as in **10l**. The two exceptions are compounds **10d** and **10f**. In compound **10d**, the lowest singlet excited state is a spectroscopically dark $^1n\pi^*$-type state that is localized on the anthraquinone moiety. In compound **10f**, on the other hand, the ordering of the lowest two singlet states is inverted with respect to compound **10l**: in **10f**, the dark $^1\pi\pi^*$ state lies vertically below the bright $^1\pi\pi^*$ state. Furthermore, in compound **10f**, both these states are strongly polar due to donor-to-acceptor CT. Furthermore, for all compounds in the series, the SCS-ADC(2) calculations predict that the lowest triplet excited state (T_1) lies vertically below the lowest singlet excited state (S_1). The lowest singlet–triplet energy gap (ΔE_{ST}) was found for compound **10d** (0.24 eV).

In all cases, the HOMO is predominantly distributed over the electron-donating tertiary amine group, whereas the LUMO is largely localized on the electron-accepting phenazine group (Supporting Information, Figures S1–S14). Thus, the bridging of the electron-donating and -accepting groups with a nonaromatic seven-membered ring achieves our aim of enforcing a spatial separation between the HOMO and the LUMO orbitals.

Having examined the relevant excited electronic states of compounds **10a**–**10n** through the lens of ab initio calculations, we are now prepared to discuss the results of the spectroscopic measurements. We begin with their photo-absorption and steady-state fluorescence spectra in organic solvents (for plots of the spectra see the Supporting Information, Figure S15). Interestingly, the hybrid ^{1}LE (toluene) and ^{1}CT (dichloromethane (DCM)/tetrahydrofuran (THF)) character of the emission was observed, as we have not noticed a dramatic bathochromic shift as a function of the polarity of solvents. The closer inspection into the emission profile through the entire set of compounds showed a significant red-shift with respect to the enlarged π-conjugation (**10a** λ_{em} 505 nm vs **10b** λ_{em} 534 nm) as well as enhanced electron-deficiency. The latter influence was clearly visible for the molecules equipped with the anthraquinone unit (**10d**, λ_{em} 628 nm), 1-azaphenazine moiety (**10e**, λ_{em} 527 nm), and most prominent for the nitrile groups (**10f**, λ_{em} 630 nm), accompanied by the displayed orange-to-red emission (Supporting Information, Figure S15). The largest red-shift noticed for **10f** would imply its increased rigidity in the excited state. The impact of the alkyl as well as halogen groups proved to be less impressive and was demonstrated in detail in Figure S15 (Supporting Information).

The emissive properties of compounds in **10a**–**10n** were subsequently investigated by time-resolved luminescence spectroscopy performed in nonpolar Zeonex as the stage between solution and solid-state (its use is aimed at the initial screening of photophysical properties allowing the probability of aggregation in the solid-state moiety to be decreased) and 4,4′-bis(N-carbazolyl)-1,1′-biphenyl (CBP) as the host matrixes (Figure 4; Supporting Information, Figures S17–S20, section SI-5). For the entire series of analyzed compounds (**10a**–**10n**), the groups affect the singlet ^{1}CT energy state, where the triplet localized energy state remains (^{3}LE). Under these circumstances, ΔE_{ST} gaps are small enough (Supporting Information, Table S3) to trigger TADF, RTP, or dual TADF and RTP. However, we turned our attention exclusively on **10d**, **f**, **g**, **h**, **m** in which the changes in photophysics emerge to be the most paramount (with respect to the character of the attached substituent). At first we paid attention to the influence of the most electron-accepting groups, nitrile (**10f**) and anthraquinone (**10d**), mounted to the scaffold of N-PAHs. For the dye **10f**, we have mixed TADF and RTP emission where the RTP contribution is higher than 1 % (Figure 4e). While tracking the emission change at different delay times (Figure 4g), distinct pure TADF emissions were observed with a microsecond delay, which is relevant for OLED devices. TADF emission starts to be visible in the μs range and circles over the ISC/rISC process to ms delay times where the RTP process is involved. Hence, for compound **10f**, the shift from TADF to pure RTP is around 0.5 ms delay time (Figure 4g) where in the Zeonex matrix dual emission is observed (Figure 4e). In the case of the second complex (**10d**), TADF was observed as delayed emission, but not from an S_1 energy state, rather a higher energy state (S_2). Such experimental findings are consistent with calculations (for more details see the Supporting Information) made for compound **10d**, as a significant f value ("bright" oscillator) for the S_2 state was determined. Nonetheless, the most intriguing behavior was observed for both **10f** and **10d** (Figure 4). Insightful analysis hints at the appearance of an inversion of singlet and triplet energy states in both cases. In the case of **10d**, the prompt fluorescence emission is a set of two signals; one with maxima at 494 nm and the second at 590 nm. The signal at 494 disappears with a circa 10 ns delay time, and only the single emission at 590 nm remains. That means our lowest singlet state is 590 nm (2.10 eV) and our real ΔEST is equal to −0.25 eV possesses $\Delta E_{ST} = -0.25$ eV (Figure 4a). A similar, but more visible observation is identified for **10f**, for which the triplet energy state is 0.34 eV higher than the lowest singlet excited state (Figure 4e). It has to be noticed, however, that the experimental values are not in accordance with those extracted from computations (Supporting Information, Table S2). The origin of negative ΔE_{ST} remains an open question and an additional, more targeted molecular design is indispensable to clearly elucidate the observed phenomena. When switched to the more electron-rich thiophene-functionalized N-PAH **10g** (with the highest triplet energy state, Figure 4i) pure TADF emission was
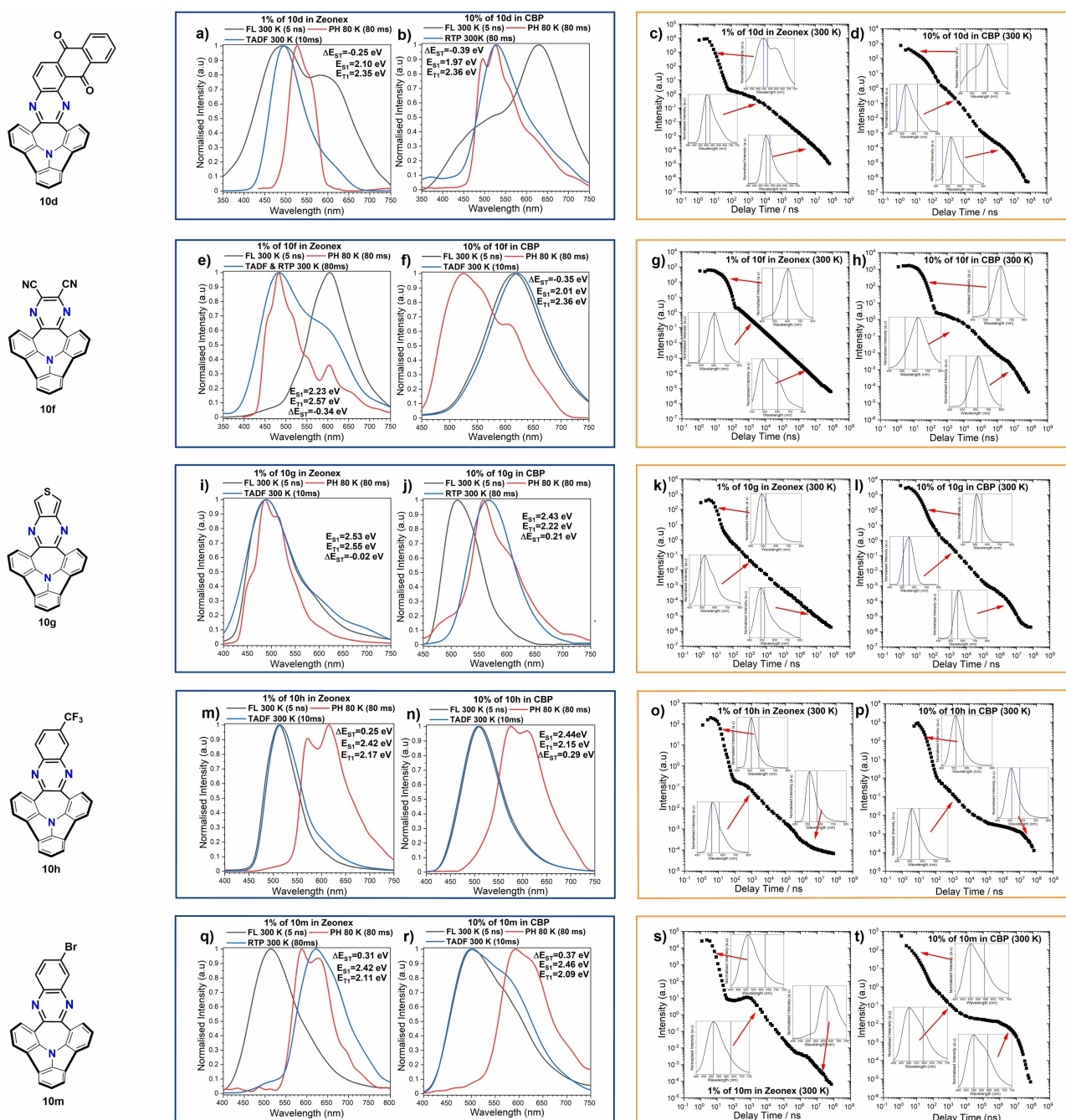
Figure 4. Time-resolved spectra of compounds **10d**, **f**, **g**, **h**, **m** in a Zeonex (a, e, i, m, q) and CBP (b, f, j, n, r) matrix. The energies correspond to the maximum emission peaks. Intensity vs delay time measurement decays with the inset spectra collected at particular delay time of compounds in Zeonex (c, g, k, o, s) and CBP matrix (d, h, l, p, t). Estimation of singlet and triplet states was done by emission.

noticed, where delayed emission (80 ms, 300 K) matches the prompt ns emission (Figure 4i).

Closer inspection of the transient curves and inset spectra at microsecond delays revealed that the spectra (Figure 4k) shift slightly to lower energies, which is not so unusual in CT-based emitters and explained by local interactions between the dipole moment of the host and the excited state dipole moment of the TADF molecule.[42] The phosphorescence part starts to be visible above 1 ms delay time. Interesting results were observed for **10h**, which

exhibit the highest DF properties; both a high PLQY value and DF/PF ratio suggest a very efficient rISC process (Table 1). The delayed emission is very strong in both the Zeonex and CBP matrix and, in both cases, the delayed emission and microsecond region match the prompt emission (Figure 4m,n), which is a TADF process. From this set of compounds, only **10m** with a single bromine group had a purely RTP emission at 80 ms delay time (Figure 4q), whereas at the microsecond range only pure TADF is observed, which means in this case we have a direct shift

Table 1: Photophysical properties of the most representative examples of N-PAHs **10d**, **f**, **g**, **h**, and **m**.

Comp.	λ_{em} [nm][a]	Host	PLQY [%][b]	τ_{PF} [ns][c]	τ_{DF} [μs][d]	τ_{Ph} [ms][d]	DF/PF[e]	S_1 [eV][f]	T_1 [eV][f]	ΔE_{ST} [eV][g]
10d	497	Zeonex	2	3.04 ± 0.04	7.43 ± 0.65	–	0.46	2.10	2.35	−0.25
	456	CBP	16	15.68 ± 0.91	2.42 ± 0.30	–	0.43	1.97	2.36	−0.39
10f	555	Zeonex	6	25.42 ± 1.12	0.94 ± 0.06	–	0.35	2.23	2.57	−0.34
	617	CBP	86	23.74 ± 1.14	1.00 ± 0.09	–	1.89	2.01	2.36	−0.35
10g	490	Zeonex	2	4.73 ± 0.38	0.96 ± 0.08	–	0.38	2.53	2.55	−0.02
	511	CBP	29	7.80 ± 0.17	0.58 ± 0.02	0.72 ± 0.07	0.18	2.43	2.22	0.20
10h	513	Zeonex	50	8.22 ± 0.88	3.99 ± 0.41	–	3.90	2.42	2.17	0.25
	507	CBP	37	9.41 ± 0.24	1.60 ± 0.11	–	5.30	2.44	2.15	0.29
10m	512	Zeonex	1	3.07 ± 0.31	1.58 ± 0.14	3.12 ± 0.23	0.73	2.42	2.11	0.31
	503	CBP	17	5.57 ± 0.36	0.79 ± 0.08	–	65.43	2.46	2.09	0.37

[a] Photoluminescence maximum. [b] Photoluminescence quantum yield. [c] Prompt fluorescence lifetime in the host. [d] Delayed emission lifetime in the host. [e] Delayed fluorescence (DF) to prompt fluorescence (PF) ratio in the host. [f] Singlet and triplet energy in host. Error ± 0.03 eV. [g] Singlet–triplet energy splitting in Zeonex. Error ± 0.05 eV.

between TADF and RTP processes rather than dual emission (Figure 4s).

In order to gauge the potential of compounds **10a–10n** as the active materials in organic light-emitting diode (OLED) structures, their photophysics were studied in the CBP (Figure 4; Supporting Information, Figures S19 and S20). It transpired that the change of the host matrix (CBP vs Zeonex) has a noticeable effect, at ms delay time, on the emission mechanisms for **10d**, **f**, and **g**. Consecutively, TADF was detected for **10f** in CBP (Figure 4f), even at the longest delay times (Figure 4h). When switched to Zeonex matrix, we anticipated singlet–triplet inversion to be observed for **10f** and similarly for **10d** (see above) but, to our surprise, the resulting effect was the opposite. For compound **10f** in Zeonex, dual TADF/RTP emission was exhibited (Figure 4e), while in the case of **10d** in Zeonex, TADF character was determined; in CBP, the emission of 10d was shifted to RTP (Figure 4a, b). Intriguingly, in both cases (Zeonex and CBP, respectively), the emission from the lowest state is not visible at longer delay times (Figure 4c, d). That means the rISC process is blocked from passing to the lowest state but the excited state follows to a higher singlet state (Zeonex) or stays on the lowest triplet energy state (CBP). A careful examination of emission decay for **10g** disclosed that the pure TADF in Zeonex (Figure 4i) changed to pure RTP in CBP (Figure 4j). If we look at the respective energy levels for **10g** (Table 1), both singlet and triplet energies are lowered but the triplet state is more affected, increasing the ΔE_{ST} to 0.20 eV. This is enough for the TADF process to be turned off and RTP promoted. For the other RTP emitter, **10m**, the RTP is observed already at μs delay times (Figure 4q), suggesting that this dye should work as RTP emitters in OLEDs. For all compounds (**10d**, **f**, and **g**), which had ΔE_{ST} in Zeonex close to 0, the gap rose significantly by at least 0.15 eV in the CBP matrix (Table 1).

For the other compounds, the change in the gap was less notable and tended to lower values in the range of 0.05 eV. Notably, one of the most important factors describing the TADF impact on the final device is the DF/PF ratio. This factor can qualify how the contribution of the triplet state contributes to the final emission. As it was stated by Dias et al.[42] above a ratio of 3 gives a 100 % use of generated triplets. In the Zeonex matrix, compounds **10b**, **e**, **h**, **i**, **j**, **k**, **l**, and **n**, showed the highest DF/PF (Supporting Information, Table S3), which demonstrates the high impact of nitrogen insertion and the halogen group to the rISC process. Even though the DF/PF ratio tends to decrease in the CBP matrix, the three compounds (**10h**, **m**, and **n**) exhibit the ratio above the threshold, and two of the compounds (**10f** and **l**) exhibit a ratio at a high value of ca. 2. As for the RTP emitters (**10d** and **g**), in both cases the overall RTP emission is much smaller than the fluorescence (0.43 and 0.18; Supporting Information, Table S3).

Prior to the device fabrication, the thermal stability for the entire set of compounds **10a–10n** was examined by using TGA/DSC techniques. We found that the vast majority of our derivatives were stable around 300 °C (for detailed results see the Supporting Information, Figures S23–S36), which agrees with behavior previously demonstrated for compounds **4a** and **4b**.[16] To our delight, such stability seems to be sufficient to maintain an efficient electroluminescence in OLED devices. In the final stage, the OLED devices were fabricated and characterized (Figure 5), and the behavior of the emitters in the CBP host was evaluated. The HOMO–LUMO values obtained from electrochemical measurement were used to evaluate the possible OLED device structures. The optimal device structure for the emitters was used in configuration: devices **10a–n** -ITO/ NPB [*N,N*′-di(1-naphthyl)-*N,N*′-diphenyl-(1,1′-biphenyl)-4,4′-diamine] (40 nm)/TSBPA [4,4′-(diphenylsilanediyl)bis-(*N,N*-diphenylaniline)] (10 nm)/10 % of **10a–n** in CBP (20 nm)/TPBi [2,2′,2′′-(1,3,5-benzinetriyl)-tris(1-phenyl-1-*H*-benzimidazole)] (50 nm)/LiF (1 nm)/Al (100 nm) (Figure 5). All the devices fabricated with the emitters except for **10d** and **10g** showed electroluminescence, which could be associated with TADF, whereas **10d** and **10g** had RTP emission, which is supported by photophysical analysis. The characteristics of the OLED devices revealed a significant increase in OLED efficiency depending on the structure (Figure 5c, d). The device based on emitter **10h** (Figure 5d) with the trifluoromethyl group was found to be the most efficient (as could be also reflected by the DF/PF ratio, see
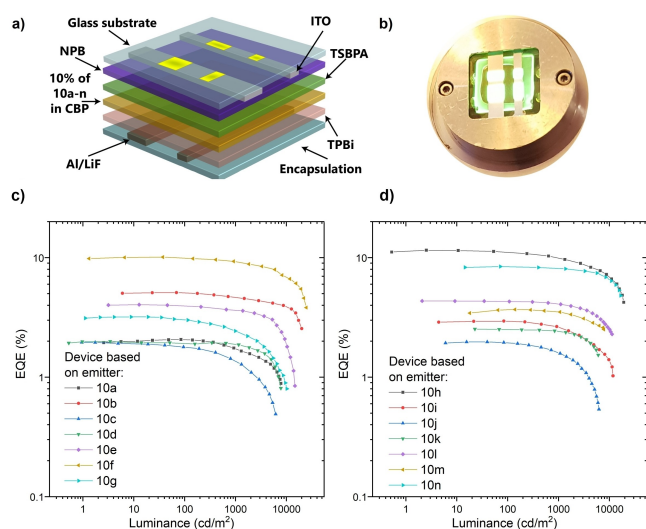
Figure 5. The characteristics of the OLED devices based on emitters **10a–n**. a) OLED structure. b) Device based on emitter **10h**. c, d) E-EQE = luminance characteristics.

above) with an external quantum efficiency (EQE) around 12% (Figure 5d).

About 10% EQE was obtained for the device based on emitter **10f** with double nitrile groups and singlet–triplet inversion effect. The highest RTP-based OLED was obtained for devices based on emitter **10g** with a thiophene unit up to 3%. All devices except **10d** (Supporting Information, Figure S37a) had an electrical turn-on voltage around 3.0 V; in the case of **10d**, the value was 2.0 V. The highest luminance was obtained for the OLED based on emitter **10f**, with up to 24680 cd m^{-2}, whereas for the RTP based OLED (**10g**), up to 10250 cd m^{-2} was recorded (Supporting Information, Figure S37a). In all the cases, the electroluminescence spectra (Supporting Information, Figure S38a, b) match the delayed emissions at the microsecond region of the time-resolved emission (Supporting Information, Figures S18 and S20). Most of the devices presented greenish emission of the OLEDs; **10g** had a yellow emission and **10f** orange-red. If we think about the molecular structure impact on the final device, the additional benzene ring allows the EQE to increase by 2.5 times (**10a** and **10b**). The insertion of the nitrogen group resulted in doubling of EQE (**10a** and **10e**) and quadrupling with the addition of a bromine group (**10a** and **10n**). Pure halogen groups had only a limited impact on the increase of the overall efficiency (lower than 2 times).

Conclusion

In conclusion, we have introduced a new paradigm for construction of strongly emitting N-doped PAHs. Our design, where N-doping is combined with a nonaromatic bridge between aromatic donor and acceptor groups, leads to superb optical and electronic properties: high photoluminescence quantum yields (PLQYs) of up to 86%, a

controlled crossover between thermally activated delayed fluorescence (TADF) and room-temperature phosphorescence (RTP), and an advantageous head-to-tail π-stacked arrangement in the molecular crystal phase. The optoelectronic properties of these nonplanar dyes can be flexibly tuned through an appropriate choice of the electron-accepting group. Showcasing their potential applicability, the N-doped PAHs were incorporated into OLED devices. The best-performing compound in the series, possessing an electron-withdrawing CF$_3$ group, shows a very high efficiency of 12%. Our findings demonstrate that the combination of N-doping and nonaromatic bridging is a general strategy towards concave PAHs with excellent optoelectronic properties. This approach could also potentially lead to compounds that exhibit singlet–triplet inversion, which is an ongoing field of research in our laboratory.

Conflict of Interest

The authors declare no conflict of interest.

Data Availability Statement

[1] A. Narita, X.-Y. Wang, X. Feng, K. Müllen, *Chem. Soc. Rev.* **2015**, *44*, 6616–6643.

[2] M. Stępień, E. Gońka, M. Żyła, N. Sprutta, *Chem. Rev.* **2017**, *117*, 3479–3716.

[3] A. Borissov, Y. K. Maurya, L. Moshniaha, W.-S. Wong, M. Żyła-Karwowska, M. Stępień, *Chem. Rev.* **2022**, *122*, 565–788.

[4] N. Bachar, L. Liberman, F. Muallem, X. Feng, K. Müllen, H. Haick, *ACS Appl. Mater. Interfaces* **2013**, *5*, 11641–11653.

[5] Q. Miao, *Adv. Mater.* **2014**, *26*, 5541–5549.

[6] C. Aumaitre, J. Morin, *Chem. Rec.* **2019**, *19*, 1142–1154.

[7] G. Hong, S. Diao, A. L. Antaris, H. Dai, *Chem. Rev.* **2015**, *115*, 10816–10906.

[8] T. Weil, T. Vosch, J. Hofkens, K. Peneva, K. Müllen, *Angew. Chem. Int. Ed.* **2010**, *49*, 9068–9093; *Angew. Chem.* **2010**, *122*, 9252–9278.

[9] C. Jung, B. K. Müller, D. C. Lamb, F. Nolde, K. Müllen, C. Bräuchle, *J. Am. Chem. Soc.* **2006**, *128*, 5283–5291.

[10] L. Schmidt-Mende, A. Fechtenkötter, K. Müllen, E. Moons, R. H. Friend, J. D. MacKenzie, *Science* **2001**, *293*, 1119–1122.

[11] K. Mullen, U. Scherf, *Organic Light Emitting Devices*, Wiley, Hoboken, **2005**.

[12] M. Hirai, N. Tanaka, M. Sakai, S. Yamaguchi, *Chem. Rev.* **2019**, *119*, 8291–8331.

[13] T. A. Schaub, K. Padberg, M. Kivala, *J. Phys. Org. Chem.* **2020**, *33*, e4022.

[14] M. Kuratsu, M. Kozaki, K. Okada, *Angew. Chem. Int. Ed.* **2005**, *44*, 4056–4058; *Angew. Chem.* **2005**, *117*, 4124–4126.

[15] H. Gilman, C. G. Stuckwisch, *J. Am. Chem. Soc.* **1943**, *65*, 1729–1733.

[16] S. Kato, T. Matsuoka, S. Suzuki, M. S. Asano, T. Yoshihara, S. Tobita, T. Matsumoto, C. Kitamura, *Org. Lett.* **2020**, *22*, 734–738.

[17] S.-N. Zou, C.-C. Peng, S.-Y. Yang, Y.-K. Qu, Y.-J. Yu, X. Chen, Z.-Q. Jiang, L.-S. Liao, *Org. Lett.* **2021**, *23*, 958–962.

[18] S. Ito, Y. Tokimaru, K. Nozaki, *Angew. Chem. Int. Ed.* **2015**, *54*, 7256–7260; *Angew. Chem.* **2015**, *127*, 7364–7368.

[19] H. Yokoi, Y. Hiraoka, S. Hiroto, D. Sakamaki, S. Seki, H. Shinokubo, *Nat. Commun.* **2015**, *6*, 8215.

[20] X. Zhang, M. R. Mackinnon, G. J. Bodwell, S. Ito, *Angew. Chem. Int. Ed.* **2022**, *61*, e202116585; *Angew. Chem.* **2022**, *134*, e202116585.

[21] Q. Li, Y. Hamamoto, G. Kwek, B. Xing, Y. Li, S. Ito, *Angew. Chem. Int. Ed.* **2022**, *61*, e202112638; *Angew. Chem.* **2022**, *134*, e202112638.

[22] M. Richter, Y. Fu, E. Dmitrieva, J. J. Weigand, A. Popov, R. Berger, J. Liu, X. Feng, *ChemPlusChem* **2019**, *84*, 613–618.

[23] N. Deng, G. Zhang, *Org. Lett.* **2019**, *21*, 5248–5251.

[24] L. Zhou, G. Zhang, *Angew. Chem. Int. Ed.* **2020**, *59*, 8963–8968; *Angew. Chem.* **2020**, *132*, 9048–9053.

[25] Y. Song, G. Zhang, *Org. Lett.* **2021**, *23*, 491–496.

[26] G. Zhu, Y. Song, Q. Zhang, W. Ding, X. Chen, Y. Wang, G. Zhang, *Org. Chem. Front.* **2021**, *8*, 727–735.

[27] S. Mishra, M. Krzeszewski, C. A. Pignedoli, P. Ruffieux, R. Fasel, D. T. Gryko, *Nat. Commun.* **2018**, *9*, 1714.

[28] M. Krzeszewski, Ł. Dobrzycki, A. L. Sobolewski, M. K. Cyrański, D. T. Gryko, *Angew. Chem. Int. Ed.* **2021**, *60*, 14998–15005; *Angew. Chem.* **2021**, *133*, 15125–15132.

[29] Z. Yang, Z. Mao, Z. Xie, Y. Zhang, S. Liu, J. Zhao, J. Xu, Z. Chi, M. P. Aldred, *Chem. Soc. Rev.* **2017**, *46*, 915–1016.

[30] M. Y. Wong, E. Zysman-Colman, *Adv. Mater.* **2017**, *29*, 1605444.

[31] X.-K. Chen, D. Kim, J.-L. Brédas, *Acc. Chem. Res.* **2018**, *51*, 2215–2224.

[32] Y. Liu, C. Li, Z. Ren, S. Yan, M. R. Bryce, *Nat. Rev. Mater.* **2018**, *3*, 18020.

[33] P. Data, Y. Takeda, *Chem. Asian J.* **2019**, *14*, 1613–1636.

[34] N. A. Kukhta, M. R. Bryce, *Mater. Horiz.* **2021**, *8*, 33–55.

[35] D. S. Surry, S. L. Buchwald, *Chem. Sci.* **2011**, *2*, 27–50.

[36] B. D. Steinberg, E. A. Jackson, A. S. Filatov, A. Wakamiya, M. A. Petrukhina, L. T. Scott, *J. Am. Chem. Soc.* **2009**, *131*, 10537–10545.

[37] J. Hu, D. Zhang, F. W. Harris, *J. Org. Chem.* **2005**, *70*, 707–708.

[38] T. G. Back, *Curr. Green Chem.* **2016**, *3*, 76–91.

[39] Y. Wu, Y. Jin, J. Xu, Y. Lv, J. Yu, *Curr. Org. Chem.* **2020**, *24*, 885–899.

[40] A. B. Trofimov, J. Schirmer, *J. Phys. B* **1995**, *28*, 2299–2324.

[41] A. Köhn, C. Hättig, *J. Chem. Phys.* **2003**, *119*, 5021–5036.

[42] F. B. Dias, T. J. Penfold, A. P. Monkman, *Methods Appl. Fluoresc.* **2017**, *5*, 012001.